



# Efficient globally optimal segmentation of cells in fluorescence microscopy images using level sets and convex energy functionals

Jan-Philip Bergeest\*, Karl Rohr

University of Heidelberg, BIOQUANT, IPMB, and DKFZ Heidelberg, Dept. of Bioinformatics and Functional Genomics, Biomedical Computer Vision Group, Im Neuenheimer Feld 267, 69120 Heidelberg, Germany

## ARTICLE INFO

### Article history:

Received 25 January 2012

Received in revised form 20 April 2012

Accepted 28 May 2012

Available online 21 June 2012

### Keywords:

Cell segmentation

Active contours

Level sets

Convex optimization

## ABSTRACT

In high-throughput applications, accurate and efficient segmentation of cells in fluorescence microscopy images is of central importance for the quantification of protein expression and the understanding of cell function. We propose an approach for segmenting cell nuclei which is based on active contours using level sets and convex energy functionals. Compared to previous work, our approach determines the global solution. Thus, the approach does not suffer from local minima and the segmentation result does not depend on the initialization. We consider three different well-known energy functionals for active contour-based segmentation and introduce convex formulations of these functionals. We also suggest a numeric approach for efficiently computing the solution. The performance of our approach has been evaluated using fluorescence microscopy images from different experiments comprising different cell types. We have also performed a quantitative comparison with previous segmentation approaches.

© 2012 Elsevier B.V. All rights reserved.

## 1. Introduction

Cell nucleus segmentation is one of the most important tasks in analyzing and quantifying fluorescence microscopy images. In particular, in high-throughput applications, semi-automatic and manual analysis are not feasible because of the enormous amount of image data. Automatic methods are needed which efficiently deal with different cell types and image artifacts such as intensity inhomogeneities.

In recent years, different approaches for the segmentation of cell nuclei in fluorescence microscopy images have been introduced. Often, thresholding approaches are applied which, however, suffer from intensity inhomogeneities within nuclei and over a whole image. To separate clustered nuclei, watershed-based techniques are frequently used. Wählby et al. (2002) proposed a watershed algorithm for cell segmentation followed by cluster splitting based on concavity regions. Lin et al. (2003) introduced an approach that uses an improved distance transform by combining the intensity gradient and a geometric distance followed by statistical model-based merging. Cheng and Rajapakse (2009) as well as Jung and Kim (2010) proposed marker-controlled watershed approaches for cluster splitting, where the optimal number of markers is determined based on the H-minima transform.

A main class of cell segmentation approaches is based on deformable models, which allow incorporation of a priori knowledge and can capture a wide spectrum of different shapes. One

can distinguish between parametric models (e.g., Kass et al., 1988) and implicit models (e.g., Osher and Sethian, 1988). *Parametric models* are based on an explicit representation of objects (e.g., Zimmer and Olivo-Marin, 2005; Wang et al., 2007; Butenuth and Heipke, 2011). Zimmer and Olivo-Marin (2005) introduced a region-based parametric energy functional which includes a coupling term for multiple contours and a penalty term to prevent merging. An extension of this approach was described by Wang et al. (2007), which includes texture-adaptive weights for the external energy of the active contour model to cope with internal pseudo-edges and low-contrast cell boundaries. In Butenuth and Heipke (2011) a combination of a parametric active contour model with a graph-based approach was introduced. However, parametric models have the disadvantage that they depend on the parameterization, an extension from 2D to 3D is difficult, and these models have problems with topological changes.

*Implicit models* using level sets have gained increased interest for cell segmentation since topological changes can be handled naturally (e.g., Ortiz de Solorzano et al., 2001; Dufour et al., 2005; Nath et al., 2006; Chang et al., 2007; Palaniappan et al., 2007; Yan et al., 2008; Maška et al., 2009; Mosaliganti et al., 2009; Padfield et al., 2009; Ersoy et al., 2009; Dzyubachyk et al., 2010; Xu et al., 2011). Ortiz de Solorzano et al. (2001) developed a two-step level set approach for segmenting cells, which employs a gradient-based energy functional. Dufour et al. (2005) introduced an energy functional which integrates multiple active contours and combines gradient-based and region-based terms. To reduce the high computational cost of representing each cell with one level set, Nath et al. (2006) introduced an approach which can cope with an arbitrary number

\* Corresponding author. Tel.: +49 6221 5451295; fax: +49 6221 54 51488.

E-mail address: [jan-philip.bergeest@bioquant.uni-heidelberg.de](mailto:jan-philip.bergeest@bioquant.uni-heidelberg.de) (J.-P. Bergeest).

of cells by using only four level sets (analogously to the four color theorem). In Chang et al. (2007) regions corresponding to single cells are determined by Voronoi tessellation and then a region-based energy functional is employed within each of these regions. Palaniappan et al. (2007) developed a level set approach based on a Bayesian energy functional which uses the flux tensor for initialization. Maška et al. (2009) first separate foreground and background of cell images using a gradient-based level set approach and second perform cluster splitting using topology preserving level sets. Mosaliganti et al. (2009) proposed an energy functional based on an appearance model of cells. Padfield et al. (2009) introduced a level set approach for cell tracking which considers tracking as a spatio-temporal volume segmentation problem and which includes size and shape constraints in the energy functional. In Dzyubachyk et al. (2010) a level set approach based on a Bayesian energy functional and a non-PDE-based minimization scheme is described. A combination of level set approaches and graph partitioning approaches within a variational framework was proposed by Ersoy et al. (2009) and Xu et al. (2011). In Ersoy et al. (2009), a multi-phase graph partitioning active contour approach using regional density functions was introduced. Xu et al. (2011) described a two-step level set approach for cell segmentation in histopathological images, where first, a geodesic active contour model is initialized by a hierarchical normalized cuts scheme and second, a level set functional is used. Whereas in graph cuts discrete optimization is employed, with level set approaches continuous optimization of the energy functionals is used. A disadvantage of previous level set approaches is that the underlying energy functionals lead to non-convex minimization problems. Hence, the optimization function has local minima and the global solution is generally not found (using local optimization methods which are typically applied). In addition, the segmentation result depends on the initialization.

In this contribution, we introduce a new approach for cell nucleus segmentation in fluorescence microscopy images which is based on active contours and level sets. Compared to previous work, our approach is based on energy functionals that lead to convex minimization problems for which global solutions are determined. We consider three functionals and take advantage of the combination of the region-based functional of Chan and Vese (2001), the Bayesian functional proposed in Rousson and Deriche (2002) which was used for cell segmentation in Dzyubachyk et al. (2010), and the region-scalable fitting energy functional introduced in Li et al. (2008). A convex formulation for the region-based functional of Chan and Vese (2001) was derived in Goldstein et al. (2010) and we employ this scheme for splitting clustered cell nuclei. In addition, we use the Bayesian functional of Rousson and Deriche (2002) and the region-scalable fitting energy functional introduced in Li et al. (2008) to cope with intensity inhomogeneities. We reformulate the latter two functionals leading to convex optimization problems. For all three convex functionals we propose an efficient minimization scheme using the Split Bregman method. Based on the convex functionals, we developed a three-step approach and a two-step approach for cell nucleus segmentation. The three-step approach (Bergeest and Rohr, 2011) combines the convex region-based Chan–Vese functional and the convex Bayesian functional, and can cope with global intensity inhomogeneities. In this contribution, we also introduce a new two-step approach which combines the convex Bayesian functional and the convex region-scalable fitting energy functional. An advantage of the two-step approach is that it can cope with both global and local intensity inhomogeneities. This allows to further improve the segmentation result. Another advantage is that only two steps are necessary compared to the three-step approach. We have successfully applied the two-step and three-step approach to 2D fluorescence microscopy images from four different

experiments comprising different cell types, and we have compared the results with previous approaches.

## 2. Cell nuclei segmentation

Our approach for the segmentation of cell nuclei in fluorescence microscopy images is based on three energy functionals. In this section, we first describe the original non-convex formulation of the functionals. Then, we introduce a reformulation as convex optimization problem and we suggest an efficient numerical technique for finding the solution.

### 2.1. Non-convex energy functionals

The first functional used in our approach is the region-based energy functional proposed by Chan and Vese (2001):

$$E_1(\Theta, \partial\Omega) = \lambda \left( \sum_{i=0}^1 \kappa_i \int_{\Omega_i} (I(\mathbf{x}) - \mu_i)^2 d\mathbf{x} \right) + \text{Per}(\Omega_1) \quad (1)$$

with  $\Theta = (\mu_0, \mu_1)$ , where  $\mu_0$  and  $\mu_1$  are the mean intensities of the background region  $\Omega_0$  and the foreground region  $\Omega_1$ , respectively.  $\partial\Omega$  denotes the boundaries between the regions  $\Omega_i$ ,  $I(\mathbf{x})$  is the image intensity at position  $\mathbf{x}$ ,  $\text{Per}(\Omega_1)$  is the perimeter of  $\Omega_1$ , and  $\kappa_0, \kappa_1, \lambda$  are weighting factors.

The second functional has been proposed in Rousson and Deriche (2002) and was derived based on a Bayesian approach:

$$E_2(\Theta, \partial\Omega) = \lambda \left( \sum_{i=0}^1 \int_{\Omega_i} -\log P(I(\mathbf{x})|\Omega_i) d\mathbf{x} \right) + \text{Per}(\Omega_1), \quad (2)$$

with  $\Theta = (\mu_0, \mu_1, \sigma_0, \sigma_1)$ , where  $\mu_i$  and  $\sigma_i$  are the mean intensities and standard deviations of the regions  $\Omega_i$ .  $P(I(\mathbf{x})|\Omega_i)$  is the conditional probability that pixel  $\mathbf{x}$  with intensity  $I(\mathbf{x})$  belongs to region  $\Omega_i$ . Here, we assume a Gaussian distribution

$$P(I(\mathbf{x})|\Omega_i) = \frac{1}{\sqrt{2\pi}\sigma_i} e^{-\frac{(I(\mathbf{x})-\mu_i)^2}{2\sigma_i^2}}.$$

An advantage of  $E_2$  compared to  $E_1$  is that the weights  $\kappa_0$  and  $\kappa_1$  are not needed, but are implicitly included via the standard deviations  $\sigma_i$ , which are estimated from the image data.

The third functional we use in our approach was introduced in Li et al. (2008) and is called region-scalable fitting energy:

$$E_3(\Theta, \partial\Omega) = \lambda \left( \sum_{i=0}^1 \kappa_i \int_{\Omega_i} \int_{\Omega_i} K_\sigma(\mathbf{x} - \mathbf{y}) |I(\mathbf{y}) - f_i(\mathbf{x})|^2 d\mathbf{y} d\mathbf{x} \right) + \text{Per}(\Omega_1), \quad (3)$$

with  $\Theta = (f_0(\mathbf{x}), f_1(\mathbf{x}))$ , where  $f_0(\mathbf{x})$  and  $f_1(\mathbf{x})$  approximate the image intensities locally in a region centered at the position  $\mathbf{x}$  in  $\Omega_0$  and  $\Omega_1$ , respectively.  $K_\sigma$  is chosen to be a Gaussian kernel

$$K_\sigma(\mathbf{u}) = \frac{1}{\sqrt{2\pi}\sigma} e^{-\frac{|\mathbf{u}|^2}{2\sigma^2}}$$

with scale parameter  $\sigma > 0$ . The scale parameter  $\sigma$  is used to control the size of the region in which the image intensities are approximated (local mean value). The center of the region is at the position  $\mathbf{x}$ . The intensity information is exploited locally due to the strong decrease of  $K_\sigma(\mathbf{x} - \mathbf{y})$  to zero as the distance between  $\mathbf{y}$  and  $\mathbf{x}$  increases. An advantage of  $E_3$  is that for each position a locally varying mean value is computed. This is different to  $E_1$  and  $E_2$ , where only global mean values are taken into account. Note that for  $\sigma \rightarrow \infty$  the energy  $E_3$  converges to the energy  $E_1$  since the local mean values  $f_i$  in  $E_3$  converge to the global mean values  $\mu_i$  in  $E_1$ .

Using a level set representation for  $E_1$ ,  $E_2$ , and  $E_3$  and applying the Euler–Lagrange equation leads to the gradient flow for the level set function  $\phi$

$$\frac{\partial \phi(\mathbf{x})}{\partial t} = \left( -\lambda r_j + \nabla \cdot \frac{\nabla \phi}{|\nabla \phi|} \right) H'(\phi(\mathbf{x})), \quad (4)$$

with  $H'(x)$  being the derivative of the Heaviside function  $H(x) = \{0 \text{ if } x < 0, 1 \text{ if } x \geq 0\}$ . The term  $r_j$  corresponds to the external image forces of the three energies  $E_j$ ,  $j = 1, 2, 3$ , and is defined as

$$r_1 = \kappa_1 (I(\mathbf{x}) - \mu_1)^2 - \kappa_0 (I(\mathbf{x}) - \mu_0)^2 \quad (5)$$

$$r_2 = \log P(I(\mathbf{x})|\Omega_1) - \log P(I(\mathbf{x})|\Omega_0) \quad (6)$$

$$r_3 = \kappa_1 \int K_\sigma(\mathbf{y} - \mathbf{x}) |I(\mathbf{x}) - f_1(\mathbf{y})|^2 d\mathbf{y} - \kappa_0 \int K_\sigma(\mathbf{y} - \mathbf{x}) |I(\mathbf{x}) - f_0(\mathbf{y})|^2 d\mathbf{y} \quad (7)$$

The parameter vector  $\theta$  can be computed directly:

$$\begin{aligned} \mu_0 &= \frac{\int I(\mathbf{x})(1 - H(\phi(\mathbf{x}))) d\mathbf{x}}{\int (1 - H(\phi(\mathbf{x}))) d\mathbf{x}} & \mu_1 &= \frac{\int I(\mathbf{x})H(\phi(\mathbf{x})) d\mathbf{x}}{\int H(\phi(\mathbf{x})) d\mathbf{x}} \\ \sigma_0^2 &= \frac{\int (I(\mathbf{x}) - \mu_0)^2 (1 - H(\phi(\mathbf{x}))) d\mathbf{x}}{\int (1 - H(\phi(\mathbf{x}))) d\mathbf{x}} & \sigma_1^2 &= \frac{\int (I(\mathbf{x}) - \mu_1)^2 H(\phi(\mathbf{x})) d\mathbf{x}}{\int H(\phi(\mathbf{x})) d\mathbf{x}} \\ f_0(\mathbf{x}) &= \frac{K_\sigma(\mathbf{x}) * [(1 - H(\phi(\mathbf{x})))I(\mathbf{x})]}{K_\sigma(\mathbf{x}) * (1 - H(\phi(\mathbf{x})))} & f_1(\mathbf{x}) &= \frac{K_\sigma(\mathbf{x}) * [H(\phi(\mathbf{x}))I(\mathbf{x})]}{K_\sigma(\mathbf{x}) * H(\phi(\mathbf{x}))}, \end{aligned}$$

where  $*$  denotes the convolution.

## 2.2. Convex energy functionals

In Chan et al. (2006), it was shown that certain non-convex minimization problems can be reformulated as convex problems. There, a convex formulation for  $E_1$  in (1) was derived. In our approach, we use this formulation and we also derive convex formulations for  $E_2$  in (2) and for  $E_3$  in (3). Following Chan et al. (2006), the Heaviside function in (4) is omitted since (4) and the following gradient descent equation have the same steady state solution

$$\frac{\partial \phi(\mathbf{x})}{\partial t} = -\lambda r_j + \nabla \cdot \frac{\nabla \phi}{|\nabla \phi|}. \quad (8)$$

Then, the corresponding energy functional can be stated as

$$E_j(\theta, \phi) = \lambda \langle \phi, r_j \rangle + |\nabla \phi|_1, \quad (9)$$

where  $\langle \cdot, \cdot \rangle$  denotes the inner product,  $|\cdot|_1$  is the L1-norm, and  $|\nabla \phi|_1$  corresponds to  $\text{Per}(\Omega_1)$ . This energy is homogenous of degree 1 in  $\phi$  (which means that if  $\phi$  is multiplied by a factor then the energy scales by the same factor), and thus does not have a minimizer in general. However, a global minimum can be guaranteed by restricting  $\phi$  to lie in a finite interval, e.g.  $[0, 1]$ , and by solving the following convex problem for the normalized  $\phi_n$ :

$$\min_{0 \leq \phi_n \leq 1} E_j^c(\theta, \phi_n) = \lambda \langle \phi_n, r_j \rangle + |\nabla \phi_n|_1 \quad (10)$$

Based on the solution  $\phi_n(\mathbf{x})$ , the segmentation result  $\Omega$  is determined by comparing the level set function with a threshold  $\alpha \in [0, 1]$ :

$$\Omega = \{\mathbf{x} : \phi_n(\mathbf{x}) > \alpha\} \quad (11)$$

## 2.3. Split Bregman method

To solve the minimization problem (10), we use the Split Bregman method. This method is a general technique for efficiently solving L1-regularized problems and for iteratively finding extrema of convex functionals (Goldstein et al., 2010). The method consists of variable splitting and Bregman iteration. Variable splitting is achieved by introducing the auxiliary vector  $\mathbf{d}$  (with dimension according to the image domain) and by using a quadratic penalty term to enforce the constraint  $\mathbf{d} = \nabla \phi_n$ . For (10) this leads to

$$(\phi_n^*, \mathbf{d}^*) = \arg \min_{0 \leq \phi_n \leq 1, \mathbf{d}} \left( \lambda \langle \phi_n, r_j \rangle + |\mathbf{d}|_1 + \frac{\nu}{2} |\mathbf{d} - \nabla \phi_n|_2^2 \right), \quad (12)$$

where  $\phi_n^*$  and  $\mathbf{d}^*$  denote the iteratively computed solution, and  $\nu$  is a weighting factor. In (12),  $\nabla \phi_n$  is no longer associated with the L1-norm, however, the constraint  $\mathbf{d} = \nabla \phi_n$  is only weakly enforced. To enforce the constraint exactly, the Bregman iteration technique is applied. With this technique a vector  $\mathbf{b}$  is included in the penalty function and an alternating minimization is carried out:

$$(\phi_n^k, \mathbf{d}^k) = \arg \min_{0 \leq \phi_n \leq 1, \mathbf{d}} \left( \lambda \langle \phi_n, r_j \rangle + |\mathbf{d}|_1 + \frac{\nu}{2} |\mathbf{d} - \nabla \phi_n - \mathbf{b}^{k-1}|_2^2 \right), \quad (13)$$

$$\mathbf{b}^k = \mathbf{b}^{k-1} + \nabla \phi_n^k - \mathbf{d}^k, \quad (14)$$

where  $\phi_n^k$  and  $\mathbf{d}^k$  represent the solution at iteration  $k$ . The problem in (13), (14) is first solved w.r.t.  $\phi_n$ , while  $\mathbf{d}$  and  $\mathbf{b}$  are fixed and second w.r.t.  $\mathbf{d}$ . In our case, we use a fast iterative Gauss-Seidel solver for the first minimization. The second minimization is obtained explicitly using the vector-valued shrinkage operator:

$$\mathbf{d}^k = \max\{|\mathbf{b}^{k-1} + \nabla \phi_n^k|_2 - \nu, 0\} \frac{\mathbf{b}^{k-1} + \nabla \phi_n^k}{|\mathbf{b}^{k-1} + \nabla \phi_n^k|_2} \quad (15)$$

## 2.4. Globally optimal cell segmentation

### 2.4.1. Three-step approach

We have developed a three-step approach for cell nuclei segmentation by combining the two convex energy functionals  $E_1^c$  and  $E_2^c$  in (10). The convex Bayesian functional  $E_2^c$  is used to deal with intensity inhomogeneities over the whole image and to segment cell nuclei with varying intensities. The convex region-based Chan-Vese functional  $E_1^c$  is used to split cell nuclei which have been falsely merged using  $E_2^c$  and is minimized independently for all regions that were segmented using  $E_2^c$ . Note, that doing this we use multiple level sets for the segmentation of an image. This is similar to multiple level set approaches (e.g., Dufour et al., 2005; Nath et al., 2006; Yan et al., 2008; Ersoy et al., 2009; Mosaliganti et al., 2009). However, in our case we do not need a coupling term to prevent level sets from merging because we perform the minimization within previously segmented regions.

Our approach consists of three steps (see Fig. 1). In the first step, we perform a segmentation of the whole image using the convex Bayesian functional  $E_2^c$ . Since this functional comprises parameters for both the mean intensities and the variances of objects we can deal with varying background intensities and with cell nuclei with varying intensities. The weighting parameter  $\kappa_1$  used in the convex region-based Chan-Vese functional  $E_1^c$  is implicitly included in  $E_2^c$  since  $\kappa_1$  is inversely proportional to the foreground variance

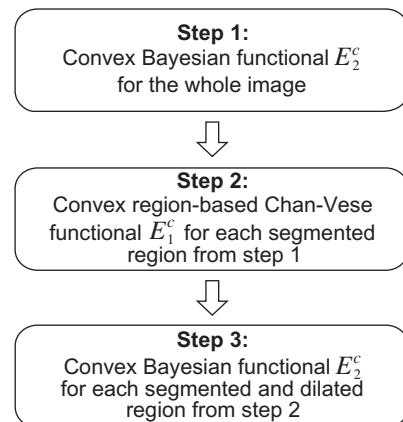


Fig. 1. Diagram of the three-step approach.



$\kappa_1 \sim 1/\sigma_1^2$ . In the case of large variances  $\sigma_1^2$  the weighting parameter  $\kappa_1$  becomes very small. A small weighting factor keeps the energy small and allows coping with cell nuclei with varying intensities. However, cell nuclei that are close to each other are likely to be merged in this step (see Fig. 2b) since varying intensities are hardly penalized. To cope with merging in the second step, we minimize  $E_1^c$  for each of the segmented cell nuclei regions in the first step. For the weighting parameters  $\kappa_0$  and  $\kappa_1$  for the background and foreground, respectively, we used the same value, i.e.,  $\kappa_0 = \kappa_1$ , such that the intensity variances of the background and foreground are equally weighted. While  $E_2^c$  allows high variances in the foreground region (e.g., intensity valleys between adjacent cell nuclei)  $E_1^c$  favors homogeneous foreground regions. This enables splitting of clustered cell nuclei (see Fig. 2c). In the third step, we use  $E_2^c$  again but this time for the segmented objects from the second step within a region-of-interest around an object (somewhat enlarged bounding box of a cell nuclei using dilation). The third step is necessary because the second step cannot deal with inhomogeneities within cell nuclei. The result of the third step in Fig. 2d shows that the segmentation at the border of the nuclei is more accurate and smoother compared to the result after the second step. Note, that if we would use  $E_2^c$  in the second step, then clustered nuclei could not be separated because the contrast in the region between the cells is not large enough (see Fig. 3b).

#### 2.4.2. Two-step approach

The three-step approach described above based on  $E_1^c$  and  $E_2^c$  can cope with global intensity inhomogeneities within the whole image. This approach can be improved by using the convex region-scalable fitting functional  $E_3^c$  in (3) in the first step instead of  $E_2^c$ , yielding a new three-step approach. The reason for the improvement is that  $E_3^c$  can deal better with both local and global intensity inhomogeneities. However, from our experiments we found that two steps are sufficient. The reason is that  $E_3^c$  yields comparable or even better results than subsequent application of  $E_2^c$  and  $E_1^c$ . Thus, we suggest a new two-step approach (see Fig. 4). In the first

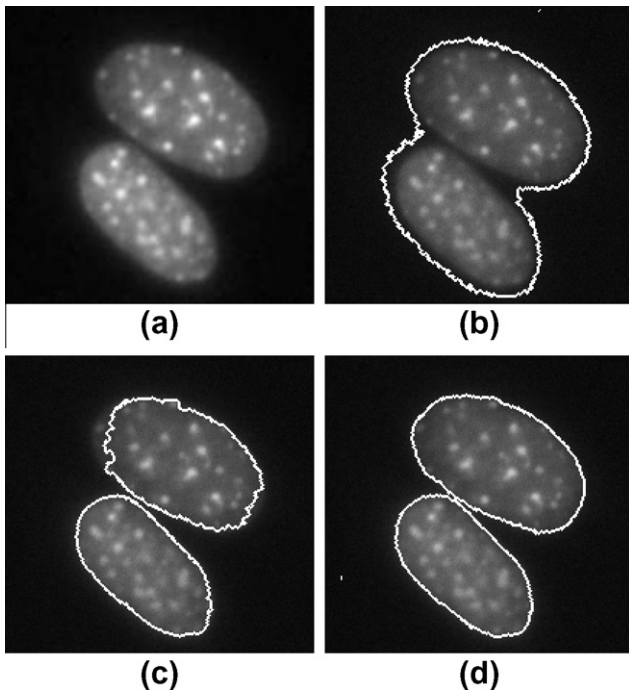


**Fig. 2.** Segmentation results of the three-step approach (contour overlay with original images): (a) Original image, (b) result after the first step, (c) after the second step, and (d) after the third step.

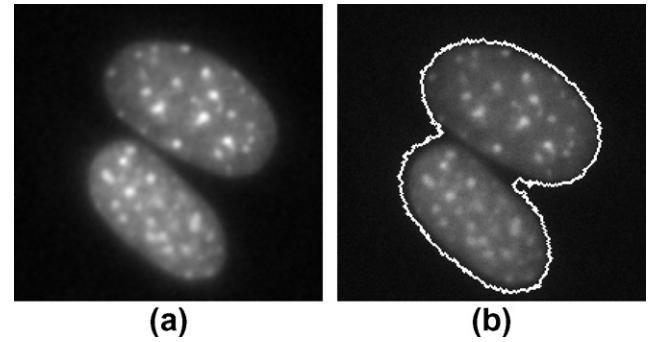


**Fig. 3.** (a) Original image and (b) segmentation result when using  $E_2^c$  in the second step of the three-step approach.

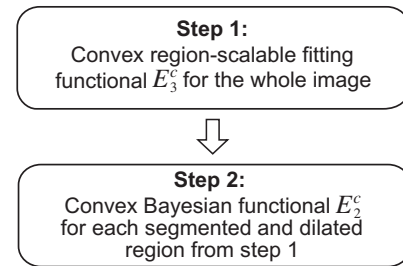


**Fig. 4.** Diagram of the two-step approach.

step, we perform a segmentation of the whole image using the convex region-scalable fitting functional  $E_3^c$ . Since the functional  $E_3^c$  takes into account locally varying mean intensities, we can deal with varying background intensities and with clustered cell nuclei that would have been merged using  $E_2^c$  and  $E_1^c$  subsequently as in the three-step approach (see Figs. 5 and 6). In the second step, we minimize the convex Bayesian functional  $E_2^c$  in a region-of-interest around an object (somewhat enlarged bounding box using dilation). The second step is used because the first step cannot cope well with inhomogeneities at the border of cell nuclei (see Fig. 5c and note the non-smooth contours of the segmented regions which do not well agree with the borders of the cell nuclei). At the same time the sensitivity of  $E_3^c$  to inhomogeneities within cell nuclei allows effective handling of clustered cells. Using  $E_3^c$ , even small intensity differences in a small region between two neighboring cell nuclei or overlapping cell nuclei make cell splitting feasible.

### 3. Experimental results

We have applied our approach to 2D fluorescence microscopy images of cell nuclei from four different experiments comparing four different cell types. We used two data sets from Coelho et al. (2009) for which ground truth is available. The first data set consists of 48 images with a size of  $1349 \times 1030$  pixels which include in total 1831 U2OS Hoechst stained cell nuclei (see Fig. 7a). The second data set contains 49 images with a size of  $1344 \times 1024$  pixels comprising in total 2178 NIH3T3 Hoechst stained nuclei (Fig. 7b). Note, that several images in the second data set are heavily affected by intensity inhomogeneities and visible artifacts. Therefore, automatic analysis of the second set is more challenging compared to the images in the first set. Furthermore, we have applied our approach to a data set of 7 2D fluorescence microscopy images of mouse neuroblastoma cells from Yu et al. (2010). Each image has a size of  $1392 \times 1040$  pixels and the data set includes in total 389 N1E115 DAPI stained cell nuclei (Fig. 7c). The ground truth for these images was obtained by

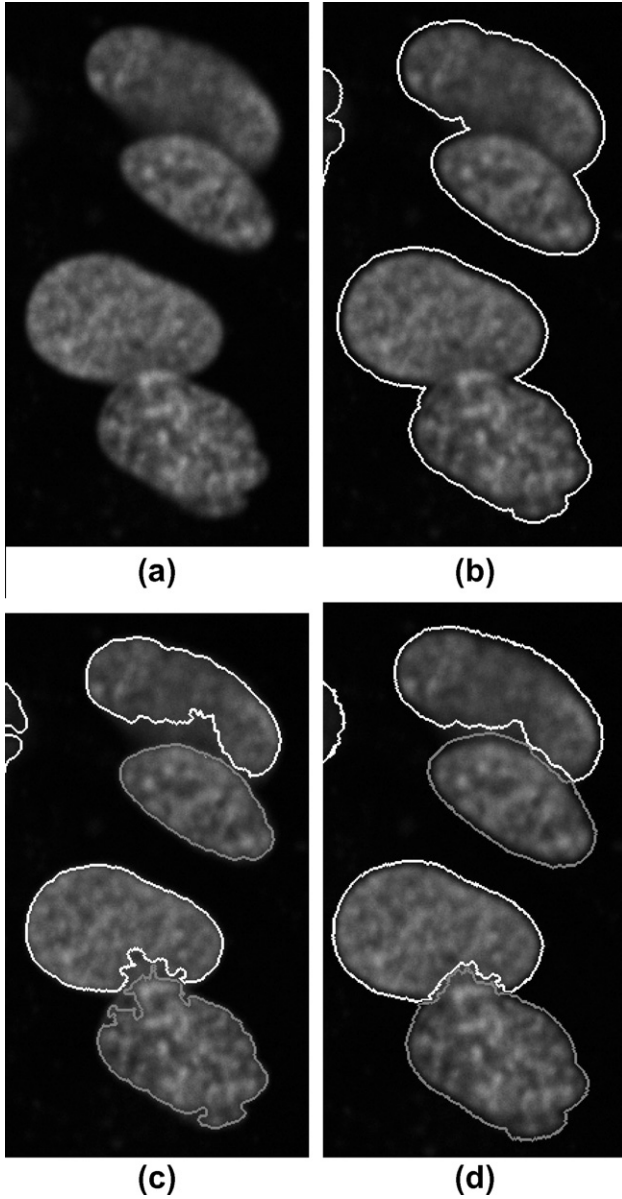


**Fig. 5.** Segmentation results of the three-step and the two-step approach (contour overlay with original images): (a) Original image, (b) three-step approach, (c) two-step approach after the first step, and (d) after the second step. For better visibility, in (c) and (d) the contours of adjacent cells have been displayed with different gray values.

manually outlining the cell nuclei borders. In addition, we have applied our approach to the data set of *Drosophila* cells used in Jones et al. (2005) for which ground truth is available. The data set consists of 16 images with a size between  $400 \times 400$  and  $512 \times 512$  pixels and includes approximately 1280 cell nuclei (Fig. 7d).

To evaluate the performance of our approach, we determined region-based and contour-based measures. As region-based measure we used the Dice coefficient and as contour-based measures we employed the normalized sum of distances (NSD, Coelho et al. (2009)) and the Hausdorff distance. The Dice coefficient is defined as

$$Dice(R, S) = \frac{2|R \cap S|}{|R| + |S|}, \quad (16)$$

where  $R$  is the binary reference image, and  $S$  is the binary segmented image. The NSD is defined as

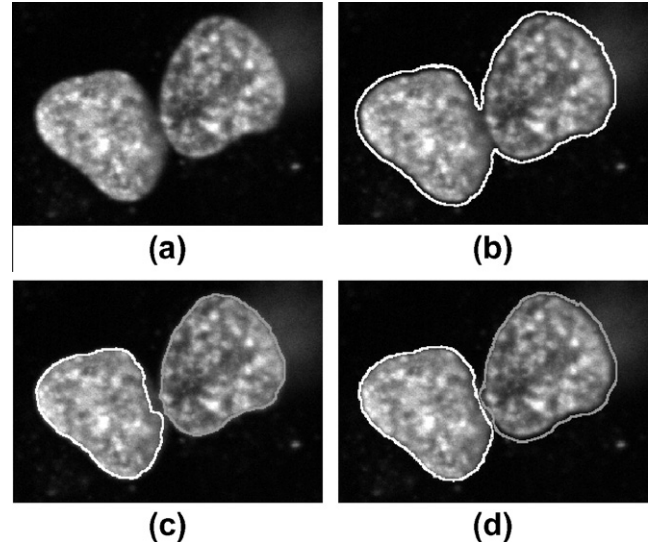


**Fig. 6.** Segmentation results of the three-step and the two-step approach (contour overlay with original images): (a) Original image, (b) three-step approach, (c) two-step approach after the first step, and (d) after the second step.

$$NSD(R, S) = \frac{\sum_{i \in R \cup S} D(i)}{\sum_{i \in R \cup S} D(i)}, \quad (17)$$

where  $D(i)$  is the minimal Euclidean distance of pixel  $i$  to the contour of the reference object. The Hausdorff distance is defined as

$$h(R, S) = \max_{i \in S_c} \{D(i)\}, \quad (18)$$

with  $S_c$  being the contour of the segmented object. We also used two detection measures, namely the number of false positives (FP) and the number of false negatives (FN). FP corresponds to spuriously segmented nuclei and FN corresponds to nuclei that have not been segmented. In all our experiments, we used for the three-step approach (Section 2.4.1) the parameter values  $\nu = 10$  and  $\kappa_0 = \kappa_1 = 1$  in (13) and (14). In the first and second step of the three-step approach we used  $\lambda = 10,000$ , and in the third step we chose  $\lambda = 1000$ . For the two-step approach (Section 2.4.2), in all our experiments we used in the first step  $\nu = 0.5$  and  $\lambda = 100$ , and in the second step  $\nu = 10$  and  $\lambda = 1000$ . The values for  $\lambda$  and  $\nu$  were chosen empirically based on a subset of the data and yielded the best results. The scale parameter  $\sigma$  was chosen empirically based on the observed average size of cell nuclei. For the U2OS, NIH3T3, and N1E115 data sets we used  $\sigma = 16$  and for the *Drosophila* data set we chose  $\sigma = 3$ . Note, that for the *Drosophila* data set, the resolution of the images is much smaller compared to the other three data sets. Therefore, the cells are much smaller in the images and a smaller value for the scale parameter is better suited. For the U2OS and NIH3T3 data sets we used a dilation of the segmented regions by  $d = 28$  (step 3 of the three-step approach and step 2 of the two-step approach), and for the N1E115 and *Drosophila* data sets we used  $d = 5$ . To initialize the minimization scheme we used the image intensities normalized with respect to the maximum intensity.

Table 1 shows the results of our three-step and our two-step approach for the different performance measures averaged over all images in the U2OS and NIH3T3 data sets. Table 2 shows the results averaged over all images in the N1E115 and *Drosophila* data sets. As a comparison, we also give the results for Otsu thresholding (Otsu, 1979) as well as for the watershed algorithm (Vincent and Soille, 1991) and the merging algorithm (Lin et al., 2003) applied to the mean thresholded image. The latter approach uses an improved watershed algorithm followed by statistical model-based

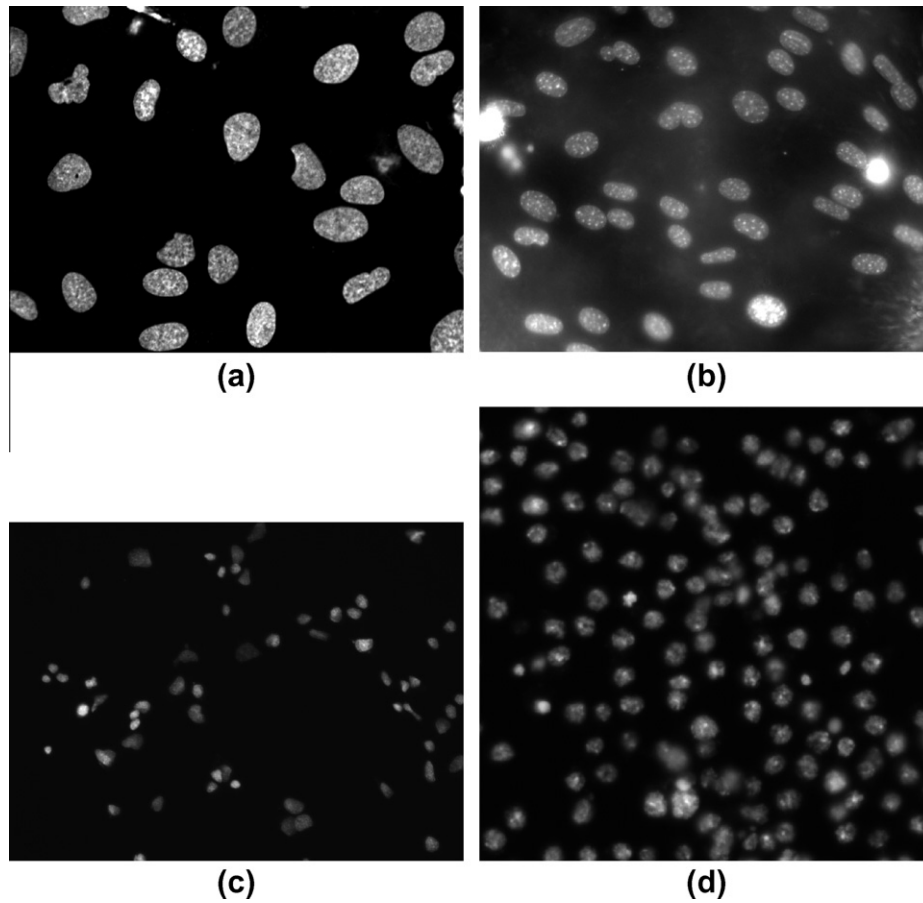


Fig. 7. Original images of the four different data sets. (a) U2OS cells, (b) NIH3T3 cells, (c) N1E115 cells, (d) Drosophila cells.

Table 1

Quantitative results for U2OS and NIH3T3 data sets for the different approaches.

Approach	U2OS cells (48 images)					NIH3T3 cells (49 images)				
	Dice	NSD	Hausdorff	FP	FN	Dice	NSD	Hausdorff	FP	FN
Manual	0.93	0.04	9.8	0.6	2.2	0.87	0.07	12.1	0.0	3.2
Otsu	0.87	0.12	34.8	<b>0.3</b>	5.5	0.64	0.35	36.7	1.7	26.4
Watershed	0.69	0.36	34.3	1.9	3.0	0.62	0.37	19.1	11.6	5.5
Merging algorithm	0.92	0.08	13.3	1.0	3.3	0.70	0.28	19.0	7.0	5.8
Non-convex $E_2$ in (2)	0.88	0.15	25.2	1.5	<b>2.8</b>	0.76	0.24	21.9	3.5	5.2
Convex $E_2^c$ in (10)	0.93	0.11	18.1	1.4	3.2	0.84	0.23	21.0	3.3	8.6
Non-convex $E_3$ in (3)	0.84	0.14	20.6	2.4	4.9	0.78	0.18	15.6	4.8	4.7
Convex $E_3^c$ in (10)	0.89	0.09	16.7	1.0	3.5	0.78	0.19	15.4	5.3	<b>4.7</b>
Three-step approach	0.94	0.06	13.3	0.5	3.9	0.83	0.14	16.5	<b>1.7</b>	11.3
Two-step approach	<b>0.94</b>	<b>0.05</b>	<b>12.8</b>	0.5	3.8	<b>0.85</b>	<b>0.12</b>	<b>14.2</b>	2.8	6.1

Bold values indicate the best result for the automatic approaches for a certain measure.

Table 2

Quantitative results for N1E115 and Drosophila data sets for the different approaches.

Approach	N1E115 cells (7 images)					Drosophila cells (16 images)				
	Dice	NSD	Hausdorff	FP	FN	Dice	NSD	Hausdorff	FP	FN
Manual	0.92	0.06	4.9	0.0	1.8	0.80	0.24	4.4	1.2	0.4
Otsu	0.82	0.17	10.0	4.7	8.1	0.82	0.20	5.5	9.3	4.0
Watershed	0.49	0.71	24.2	<b>0.0</b>	7.7	0.80	0.23	4.7	0.9	10.5
Merging algorithm	0.72	0.34	13.6	0.14	4.1	0.67	0.43	9.7	<b>0.0</b>	18.1
Non-convex $E_2$ in (2)	0.71	0.37	21.0	1.9	4.0	0.43	0.77	24.1	1.4	33.7
Convex $E_2^c$ in (10)	0.73	0.33	18.5	1.1	3.4	0.51	0.66	20.0	2.3	29.6
Non-convex $E_3$ in (3)	0.88	0.10	8.4	0.6	3.7	0.79	0.23	5.2	7.6	8.9
Convex $E_3^c$ in (10)	0.88	0.10	8.3	0.3	3.4	0.82	0.19	4.7	3.3	3.4
Three-step approach	0.89	0.10	8.0	0.6	5.7	0.80	0.21	4.5	2.6	7.8
Two-step approach	<b>0.90</b>	<b>0.10</b>	<b>6.7</b>	0.4	<b>3.0</b>	<b>0.82</b>	<b>0.19</b>	<b>4.0</b>	2.9	<b>3.4</b>

Bold values indicate the best result for the automatic approaches for a certain measure.



region merging to cope with oversegmentation and yielded the best results in the evaluation study of Coelho et al. (2009). Also, we included the result of the non-convex functional  $E_2$  in (2) from Rousson and Deriche (2002) which was used in Dzyubachyk et al. (2010). We also provided the result of the non-convex functional  $E_3$

in (3) from Li et al. (2008). In addition, we show the results for the convex functionals  $E_2^c$  and  $E_3^c$ . Moreover, we included the result of manual segmentation (for a subset of 5 images for each data set) by a different observer than the one who provided the ground truth (second row, “Manual”).

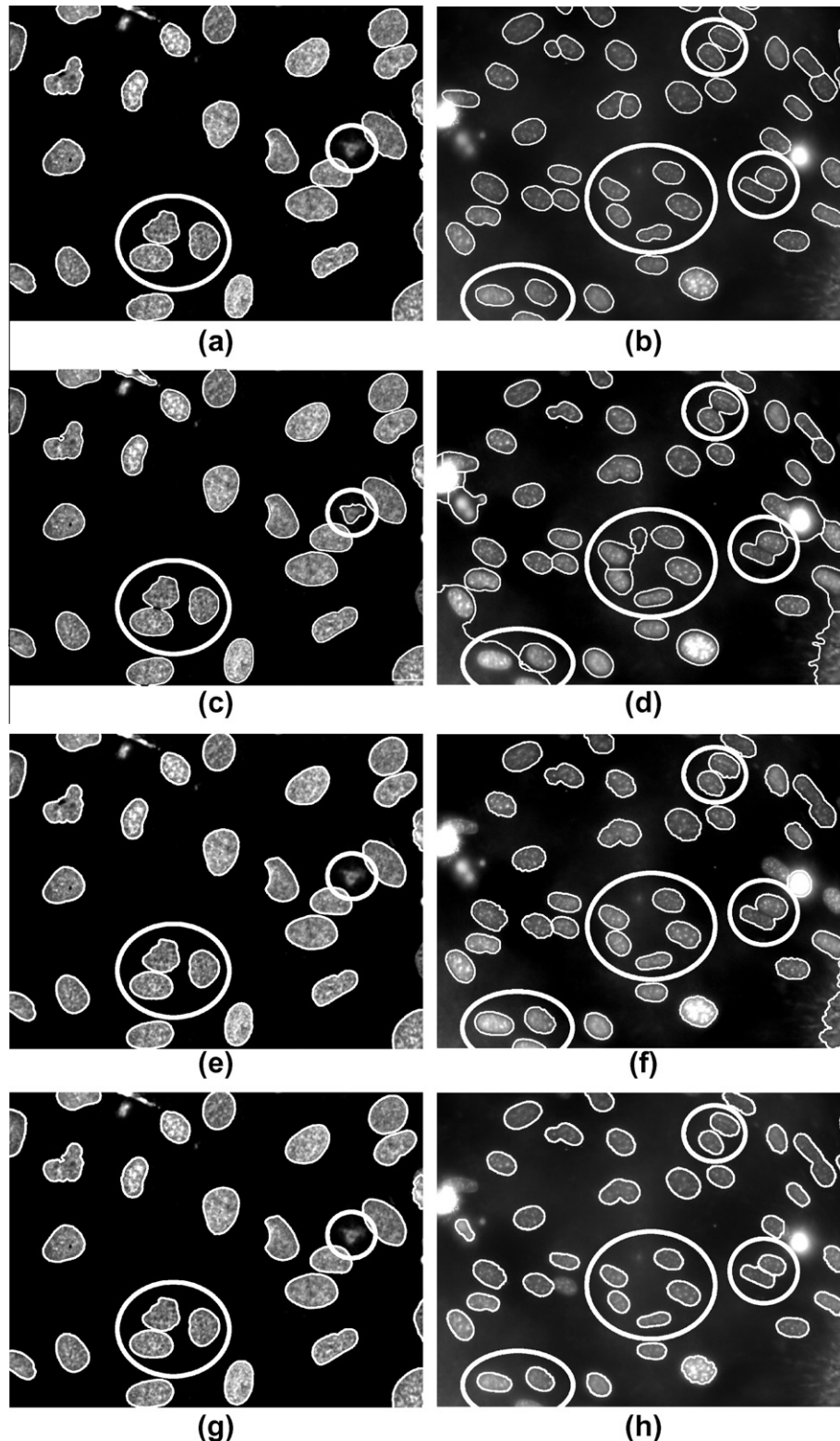


**Fig. 8.** Segmentation results of different approaches (contour overlays with original images). First column: U2OS cells, second column: NIH3T3 cells; first row: ground truth, second row: merging algorithm of Lin et al. (2003), third row: three-step approach, forth row: two-step approach.

From Table 1 it can be seen that the two-step approach yields the best results for the Dice coefficient, the NSD, and the Hausdorff distance for both data sets, and that the results are comparable to the results by the different observer (“Manual”). In particular, for the more challenging NIH3T3 images we obtain significantly better results than previous approaches. It also turns out that the two-step approach yields similar or better results than the three-step approach. Furthermore, it can be seen that the three-step and the two-step approach yield better results than the convex Bayesian functional  $E_2^c$  (which is the first step of the three-step approach and the second step of the two-step approach). Also, the two-step approach yields better results than the convex region-scalable fitting functional  $E_3^c$  (which is the first step of the two-step approach). Thus, the multiple step scheme is advantageous. In addition, it can be seen that the convex Bayesian functional  $E_2^c$  yields better results than the non-convex Bayesian functional  $E_2$ . Also, the convex region-scalable fitting functional  $E_3^c$  yields better results than the corresponding non-convex functional  $E_3$ . For the FP value the results of the three-step and two-step approach are equally good or comparable to the best results of the other approaches. Regarding the FN value, for the three-step approach we obtain for the U2OS cell images similar results as for the other approaches, while for the NIH3T3 cell images we obtain intermediate results. For both data sets, the two-step approach yields better results than the three-step approach. In particular, for the NIH3T3 images we obtain a significantly smaller FN value. While the FN value for the U2OS cell images is smaller, the FP value is somewhat higher for the NIH3T3 cell images compared to the three-step approach but it is still better than that for the merging algorithm (which yielded the best results in the evaluation study of Coelho et al. (2009)). Compared to the merging algorithm, the three-step and two-step approach allow better splitting of clustered cell nuclei, cope better with spurious objects (see Figs. 8c, e, and g), and yield more accurate results for the cell nuclei shapes (see Fig. 8d, f, and h). Compared to the three-step approach, the two-step approach can cope better with overlapping and touching cell nuclei (see Figs. 5 and 6).

The results in Table 2 for the N1E115 and Drosophila data sets are similar to those in Table 1. It can be seen that for the N1E115 cell images our three-step and two-step approach yield the best results for the Dice coefficient, the NSD, the Hausdorff distance, and that the results are comparable to those by the different observer (“Manual”). For the Drosophila data set, the two-step approach yields the best results while the results of the three-step are also good and comparable to the results by the different observer

(“Manual”). Note, that for this data set Otsu thresholding and watershed yield good results for the Dice coefficient and the NSD, however, Otsu thresholding has a relatively high FP value and watershed has a relatively high FN value. The non-convex Bayesian functional  $E_2$  and the convex functional  $E_2^c$  yield relatively poor results because the contrast between cells within large clusters often is too low and therefore the cells are merged in the segmentation. Compared to  $E_2$  and  $E_2^c$ , the non-convex and convex region-scalable fitting functionals  $E_3$  and  $E_3^c$  yield better results. For the Hausdorff distance the three-step and two-step approach yield the best results compared to previous approaches, and the two-step approach outperforms the three-step approach. Regarding the FP value, the three-step and two-step approach yield results comparable to the best result for the N1E115 data set and intermediate results for the Drosophila data set. For the FN value, the three-step and two-step approach yield the best results, and the two-step approach outperforms the three-step approach.

We also performed a sensitivity analysis of the parameters of the two-step approach (see Table 3). We applied the two-step approach to the U2OS data set and varied one parameter at a time while the other parameters were kept fixed at their default values. We studied the parameters  $\lambda$ ,  $v$ ,  $\sigma$ , and  $d$  (for the default values see the beginning of Section 3) and we used as performance measures the Dice coefficient, NSD, and the Hausdorff distance. Since we have a two-step segmentation approach we distinguish two cases: Fixed parameters in step 1 and fixed parameters in step 2. Note, that since the parameters  $\sigma$  and  $d$  are only relevant in one of the two steps, the entries in Table 3 for the corresponding other step are empty. From Table 3 it can be seen that the segmentation results are relatively insensitive to parameter variations.

In our approach, the minimization of the convex Bayesian functional  $E_2^c$  in (10) for a whole image with a size of  $1349 \times 1030$  pixels converges after about 5 iterations and the computation time is approximately 15 s per image (using an Intel Xeon CPU X5550, 2.67 GHz, with 48 GB RAM, and Linux 64 bit). In comparison, using a standard level set scheme for the non-convex Bayesian functional  $E_2$  in (2) with gradient descent optimization needs about 400 iterations and the computation time is about 9 min. For the convex region-scalable fitting functional  $E_3^c$  our approach converges after about 10 iterations (ca. 100 s) while the optimization for the non-convex functional  $E_3$  in (3) needs about 1000 iterations (ca. 35 min). Thus, our approach is significantly faster. As convergence criterion we used the average Euclidean distance between the contours of segmented objects in two successive iterations.

**Table 3**

Quantitative results for the parameter sensitivity analysis for the two-step approach. The first column shows the variation of the parameters while the other parameters are kept fixed at default values.

Parameter	Fixed parameters in step 1			Fixed parameters in step 2		
	Dice	NSD	Hausdorff	Dice	NSD	Hausdorff
$\lambda = 10$	0.935	0.064	12.63	0.939	0.063	14.20
$\lambda = 100$	0.936	0.062	12.71	0.936	0.054	12.81
$\lambda = 1000$	0.936	0.054	12.81	0.939	0.054	12.04
$\lambda = 10000$	0.938	0.059	12.84	0.932	0.062	12.07
$v = 0.01$	0.938	0.059	12.84	0.922	0.073	12.04
$v = 0.5$	0.938	0.059	12.84	0.936	0.054	12.81
$v = 5$	0.936	0.061	12.80	0.946	0.049	12.53
$v = 10$	0.936	0.054	12.81	0.946	0.047	12.52
$\sigma = 8$				0.941	0.054	12.64
$\sigma = 12$				0.938	0.056	12.31
$\sigma = 16$				0.936	0.054	12.81
$\sigma = 24$				0.941	0.056	12.74
$d = 20$	0.938	0.059	12.95			
$d = 24$	0.938	0.060	12.89			
$d = 28$	0.936	0.054	12.81			
$d = 32$	0.936	0.062	12.91			



#### 4. Discussion

We have introduced a new globally optimal approach based on active contours and level sets for cell nuclei segmentation in fluorescence microscopy images. We have developed a three-step and a two-step approach. The three-step approach employs two convex energy functionals, which are convex formulations of the region-based Chan–Vese functional and the Bayesian functional. By applying the convex functionals subsequently in three steps we can cope with global intensity inhomogeneities and neighboring cells. The two-step approach employs the convex Bayesian functional and the convex region-scalable fitting energy functional, and requires only two subsequent steps. In the first step, we use the region-scalable fitting energy functional, which can cope with spatially local mean intensity values in comparison to the region-based Chan–Vese functional and the Bayesian functional which are based on global mean intensity values. In the second step, we use the Bayesian functional which allows us to deal with inhomogeneities at the border of cell nuclei. The two-step approach can cope with both global intensity inhomogeneities and local intensity inhomogeneities. Another advantage of the two-step approach is that small intensity differences between neighboring cell nuclei or even between overlapping cell nuclei make cluster splitting feasible. A further improvement in cluster splitting could possibly be obtained by using boundary curvature information in an additional post-processing step. To minimize the convex energy functionals we use the Split Bregman method, which is an efficient method for  $L1$ -regularized problems and which significantly reduces the computation time compared to standard level set approaches. Thus, our approach is suitable for high-throughput applications and very large data sets. We have demonstrated the applicability of our approach using fluorescence microscopy image data sets from four different experiments comprising four different cell types. In total, we used 120 real microscopy images which include 5678 cells. From the experiments it turned out that both the three-step approach and the two-step approach can cope with images of different cell types. We also found that the two-step approach yields superior results compared to the three-step approach and compared to previous approaches. In future work, our approach will be applied to large-scale high-throughput applications for identifying relevant factors of cell function.

#### Acknowledgments

We thank Luis Pedro Coelho (CMU) for help with his software. Support of the BMBF projects FANCI and EpiSys (SysTec) and the EU project SysPatho (FPT) is gratefully acknowledged.

#### References

- Bergeest, J.P., Rohr, K., 2011. Fast globally optimal segmentation of cells in fluorescence microscopy images, in: Fichtinger, G., Martel, A., Peters, T. (Eds.), *Proc. Int. Conf. on Medical Image Computing and Computer Assisted Intervention (MICCAI 2011)*, Part I, Springer, Heidelberg, pp. 645–652.
- Butenuth, M., Heipke, C., 2011. Network snakes: graph-based object delineation with active contour models. *Machine Vision and Applications* 23, 1–19.
- Chan, T.F., Esedoglu, S., Nikolova, M., 2006. Algorithms for finding global minimizers of image segmentation and denoising models. *SIAM Journal on Applied Mathematics* 66, 1632–1648.
- Chan, T.F., Vese, L.A., 2001. Active contours without edges. *IEEE Transactions on Image Processing* 10, 266–277.
- Chang, H., Yang, Q., Parvin, B., 2007. Segmentation of heterogeneous blob objects through voting and level set formulation. *Pattern Recognition Letters* 28, 1781–1787.
- Cheng, J., Rajapakse, J., 2009. Segmentation of clustered nuclei with shape markers and marking function. *IEEE Transactions on Biomedical Engineering* 56, 741–748.
- Coelho, L.P., Shariff, A., Murphy, R.F., 2009. Nuclear segmentation in microscope cell images: a hand-segmented dataset and comparison of algorithms. In: *Proc. IEEE International Symposium on Biomedical Imaging (ISBI 2009)*, pp. 518–521.
- Dufour, A., Shinin, V., Tajbakhsh, S., Guillen-Aghion, N., Olivo-Marín, J.C., Zimmer, C., 2005. Segmenting and tracking fluorescent cells in dynamic 3-D microscopy with coupled active surfaces. *IEEE Transactions on Image Processing* 14, 1396–1410.
- Dzyubachyk, O., van Cappellen, W.A., Essers, J., Niessen, W.J., Meijering, E.H.W., 2010. Advanced level-set-based cell tracking in time-lapse fluorescence microscopy. *IEEE Transactions on Medical Imaging* 29, 852–867.
- Ersoy, I., Bunyak, F., Chagin, V., Cardoso, M., Palaniappan, K., 2009. Segmentation and classification of cell cycle phases in fluorescence imaging. In: Yang, G.Z., Hawkes, D.J., Rueckert, D., Noble, J.A., Taylor, C.J. (Eds.), *Proc. Int. Conf. on Medical Image Computing and Computer-Assisted Intervention (MICCAI 2009)*, Part II, Springer, Heidelberg, pp. 617–624.
- Goldstein, T., Bresson, X., Osher, S., 2010. Geometric applications of the split Bregman method: segmentation and surface reconstruction. *Journal of Scientific Computing* 45, 272–293.
- Jones, T., Carpenter, A., Golland, P., 2005. Voronoi-based segmentation of cells on image manifolds. In: *Proc. Computer Vision for Biomedical Image Applications*. Springer, pp. 535–543.
- Jung, C., Kim, C., 2010. Segmenting clustered nuclei using h-minima transform-based marker extraction and contour parameterization. *IEEE Transactions on Biomedical Engineering* 57, 2600–2604.
- Kass, M., Witkin, A., Terzopoulos, D., 1988. Snakes: active contour models. *International Journal of Computer Vision* 1, 321–331.
- Li, C., Kao, C., Gore, J., Ding, Z., 2008. Minimization of region-scalable fitting energy for image segmentation. *IEEE Transactions on Image Processing* 17, 1940–1949.
- Lin, G., Adiga, U., Olson, K., Guzowski, J.F., Barnes, C.A., Roysam, B., 2003. A hybrid 3D watershed algorithm incorporating gradient cues and object models for automatic segmentation of nuclei in confocal image stacks. *Cytometry A* 56, 23–36.
- Maška, M., Daněš, O., Ortiz-de Solórzano, C., Muñoz-Barrutia, A., Kozubek, M., García, I., 2009. A two-phase segmentation of cell nuclei using fast level set-like algorithms. *Image Analysis*, 390–399.
- Mosaliganti, K., Gelas, A., Gouaillard, A., Noche, R., Obholzer, N., Megason, S., 2009. Detection of spatially correlated objects in 3D images using appearance models and coupled active contours. In: Yang, G.Z., Hawkes, D.J., Rueckert, D., Noble, J.A., Taylor, C.J. (Eds.), *Proc. Int. Conf. on Medical Image Computing and Computer Assisted Intervention (MICCAI 2009)*, Part II, Springer, Heidelberg, pp. 641–648.
- Nath, S.K., Palaniappan, K., Bunyak, F., 2006. Cell segmentation using coupled level sets and graph-vertex coloring. In: Larsen, R., Nielsen, M., Sparring, J. (Eds.), *Proc. Int. Conf. on Medical Image Computing and Computer Assisted Intervention (MICCAI 2006)*, Part I, Springer, Heidelberg, pp. 101–108.
- Osher, S., Sethian, J., 1988. Fronts propagating with curvature-dependent speed: algorithms based on Hamilton–Jacobi formulations. *Journal of Computational Physics* 79, 12–49.
- Otsu, N., 1979. A threshold selection method from gray-level histograms. *IEEE Transactions on System, Man and Cybernetics* 9, 62–66.
- Padfield, D., Rittscher, J., Thomas, N., Roysam, B., 2009. Spatio-temporal cell cycle phase analysis using level sets and fast marching methods. *Medical Image Analysis* 13, 143–155.
- Palaniappan, K., Ersoy, I., Nath, S., 2007. Moving object segmentation using the flux tensor for biological video microscopy. *Advances in Multimedia Information Processing (PCM 2007)*, 483–493.
- Rousson, M., Deriche, R., 2002. A variational framework for active and adaptive segmentation of vector valued images. In: *Proc. Workshop on Motion and Video Computing*, IEEE Computer Society, pp. 56–62.
- Ortiz de Solórzano, C., Malladi, R., Lelievre, S., Lockett, S.J., 2001. Segmentation of nuclei and cells using membrane related protein markers. *Journal of Microscopy* 201, 404–415.
- Vincent, L., Soille, P., 1991. Watersheds in digital spaces: an efficient algorithm based on immersion simulations. *IEEE Transactions on Pattern Analysis and Machine Intelligence* 13, 583–598.
- Wählby, C., Lindblad, J., Vondrus, M., Bengtsson, E., Björkstén, L., 2002. Algorithms for cytoplasm segmentation of fluorescence labelled cells. *Analytical Cellular Pathology* 24, 101–111.
- Wang, X., He, W., Metaxas, D., Mathew, R., White, E., 2007. Cell segmentation and tracking using texture-adaptive snakes. In: *Proc. IEEE International Symposium on Biomedical Imaging (ISBI 2007)*, IEEE, pp. 101–104.
- Xu, J., Janowczyk, A., Chandran, S., Madabhushi, A., 2011. A high-throughput active contour scheme for segmentation of histopathological imagery. *Medical Image Analysis* 15, 851–862.
- Yan, P., Zhou, X., Shah, M., Wong, S.T.C., 2008. Automatic segmentation of high-throughput RNAi fluorescent cellular images. *IEEE Transactions on Information Technology in Biomedicine* 12, 109–117.
- Yu, W., Lee, H., Hariharan, S., Bu, W., Ahmed, S., 2010. Evolving generalized Voronoi diagrams for accurate cellular image segmentation. *Cytometry A* 77, 379–386.
- Zimmer, C., Olivo-Marín, J., 2005. Coupled parametric active contours. *IEEE Transactions on Pattern Analysis and Machine Intelligence* 27, 1838–1842.